Digest Journal of Nanomaterials and Biostructures Vol. 7, No. 4, October-December 2012, p. 1757-1766

PHOTOLUMINESCENCE, MAGNETIC PROPERTIES AND PHOTOCATALYTIC ACTIVITY OF Gd^{3+} DOPED ZnO NANOPARTICLES

O. OPREA*, O. R. VASILE, G. VOICU, L. CRACIUN, E. ANDRONESCU
University Politehnica of Bucharest, Faculty of Applied Chemistry and Materials Science, Romania,

Nanocrystalline ZnO particles doped with Gd(III) ions were prepared by a simple sol-gel method from methanolic solution of zinc acetate dihydrate, aqueous solution of $Gd(NO_3)_3 \cdot 9H_2O$, and starch. By calcination of the xerogel at 400°C we obtained nanopowders of ZnO doped with Gd(III) ions. The dopant percentage was increased up to 5%. Optical investigation shows that the Gd doping in ZnO lattice leads to a decrease in the near band edge position due to the introduction of new unoccupied states by Gd 4*f* electrons. The blue-green luminescence is enhanced by increasing the Gd(III) percentage. In addition, the photocatalytic activity was investigated against methylene blue.

(Received October 8, 2012; Accepted November 7, 2012)

Keywords: Gd-doped zinc oxide, Ferromagnetism, Nanomaterials, photocatalysis

1. Introduction

Semiconductor nanoparticles have attracted interests of many academic and industrial researchers because of their unusual optoelectronic properties. Wurtzite ZnO is an n-type semiconductor with a wide band-gap. Nanosized ZnO can be utilized in electrochemical fields including chemical sensors [1], photocatalysts [2, 3], phosphors [4], thin films [5] and dye-sensitized solar cells [6].

Pure zinc oxide is a degenerate semiconductor with a wide bandgap (3.3 eV) and has transparent properties in the visible range of the spectrum. Therefore, it is used in the production of many optoelectronic devices as transparent conducting oxides (TCO), like solar cells or flat panel displays. In order to improve the TCO properties of ZnO, it is usually doped with metallic ions. Doping of ZnO with magnetic transition metals (TM) creates ferromagnetic properties at room temperature (RT FM) and might form dilute magnetic semiconductors (DMSs) [7]. The suitability of DMS for spintronics applications is derived from its ability to dope a fraction of host semiconductor cations with magnetic ions. Theoretical prediction suggests that the common semiconductors doped with qualified TM in the range of several atomic percent lead to the development of the RT FM [8].

Few works were conducted on magnetic properties of rare-earth-doped ZnO [9-11].

It has been noted that the local structure and magnetic properties of doped ZnO are strongly sensitive to the preparation parameters [12]. It is known that the solid solubility of a dopant in a matrix depends on the preparation method and conditions, especially the temperature during preparation, the annealing temperature, the doping concentration, and even the matrix grain size [13,14]. Therefore, different values of solid solubility are noted in the literature.

A variety of structural defects may exist in the ZnO nanoparticles, which will influence the electronic and optoelectronic properties. The intrinsic defects commonly found in ZnO are zinc interstitials (Zn_i), zinc vacancies (V_{Zn}), oxygen interstitials (O_i), oxygen vacancies (V_O), oxygen antisites (O_{Zn}), and zinc antisites (Zn_O). A detailed description about these defects has been reported by Kohan *et al* [15].

* Corresponding author: ovidiu73@yahoo.com

ZnO have been prepared by adapting synthetic methods developed by Koch et al. [16], Bahnemann et al. [17], or Spanhel et al. [18]. We have reported [19] that nanocrystalline ZnO particles can be successfully prepared through controlled hydrolysis of zinc acetate in methanol, at low temperature, and ambient atmosphere, without using any alkaline solution.

Samples with different Gd to Zn content were synthesized by a new sol-gel method, from methanolic solution of zinc acetate dihydrate, aqueous solution of $Gd(NO_3)_3 \cdot 9H_2O$, and starch. The samples were structurally characterized by means of FTIR, UV-Vis and PL spectrometry, XRD, TEM, HRTEM and SAED.

2. Experimental procedure

Zinc acetate dihydrate, $Zn(Ac)_2 \cdot 2H_2O$ and $Gd(NO)_3 \cdot 9H_2O$ with 99.9% purity, were obtained from Merck. Absolute methanol and starch was used as received from Sigma without further purification.

ZnO synthesis

0.01 moles $Zn(CH_3COO)_2$ $2H_2O$ were dissolved in 50 mL methanol. Corresponding quantities (1, 2.5 and 5%) $Gd(NO)_3 \cdot 9H_2O$ were solved in 10mL H_2O. The solutions were poured together under magnetic stirring and 1 g of starch was slowly added (Fig. 1). The solution was heated at 60°C for 2 hrs, and then was kept for 3 days at the ambient temperature. A sample from the obtained xerogel was submitted to thermal analysis to establish the calcination temperature. From the TG curve, we choose 400°C as calcination temperature, as no mass loss was detected over this temperature. The annealing time was 2 hours. The final product obtained after calcination was a white powder. We have prepared four ZnO samples by this method with 0%, 1%, 2.5% and 5% Gd(III).

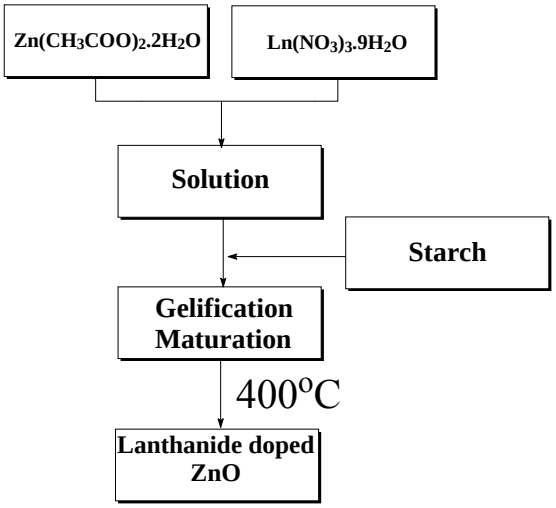

Fig. 1. The schematic process for obtaining the Gd(III) doped ZnO nanopowder.

3. Experimental techniques

a) Electron Microscope Images. The transmission electron images were obtained on finely powdered samples using a Tecnai^{TM} G^2 F30 S-TWIN high resolution transmission electron microscope from FEI, equipped with STEM/HAADF detector, EDX (Energy dispersive X-ray Analysis) and EFTEM - EELS (Electron energy loss spectroscopy) operated at an acceleration voltage of 300 KV obtained from a Shottky Field emitter with a TEM point resolution of 2 Å and line resolution of 1.02 Å.

b) X-ray Diffraction. X-ray powder diffraction patterns were obtained with a Shimadzu XRD6000 diffractometer, using Cu Kα (1.5406 Å) radiation operating with 30 mA and 40 kV in the 2θ range 10–70°. A scan rate of 1° min^{-1} was employed.

c) Infrared Spectroscopy. The Fourier transform infrared (FTIR) spectra were recorded using the KBr pellet technique on a Bruker Tensor 27 spectrometer in the 4000–400 cm^{-1} frequency range. A total of 30 scans and a resolution of 1 cm^{-1} were employed in getting the spectra.

d) Thermal analysis. Thermal behaviour of the ZnO nanopowder was followed by TG-DSC with a Netzsch TG 449C STA Jupiter. Sample was placed in alumina crucible and heated with 10K·min^{-1} from room temperature to 900° C, under the flow of 10 mL min^{-1} dried air.

e) Photoluminescence spectra. Photoluminescence spectra (PL) were measured with a Perkin Elmer P55 spectrometer using a Xe lamp as a UV light source at ambient temperature, in the range 200-800 nm, with all the samples in solid state. The measurements were made with scan speed of 200 nm·min^{-1}, slit of 10 nm, and cut-off filter of 1%. An excitation wavelength of 320 nm was used.

f) Diffuse reflectance spectra measurements were made with a JASCO V560 spectrophotometer with solid sample accessory, in the domain 200-800nm, with a speed of 200nm·min^{-1}.

g) Photocatalytic activity was determined against methylene blue (MB) solution, 10^{-4} %, by irradiation with an Hg lamp. Samples of 0.0251 g powder were inserted in 20 mL solution of MB. At defined time intervals a sample of 2mL was taken out and its UV-Vis spectra was recorded.

h) The measurements of magnetic properties were made using vibrating sample magnetometer (VSM, Lakeshore 7304, Lakeshore Cryotronics, Inc., Westerville, OH, USA).

4. Results and discussions

The thermal analysis (Fig. 2) was recorded to establish the calcination temperature for the xerogel. Up to 120°C there is a mass loss of 4.35%, accompanied by an endothermic effect, corresponding to water elimination. The next two mass loss steps (- 80.44%) correspond to combustion of starch and decomposition of organic residue and nitrate ion. Virtually no mass loss was recorded after 400°C. The residual mass (Gd(III) doped ZnO nanopowder) represent 15.34%.

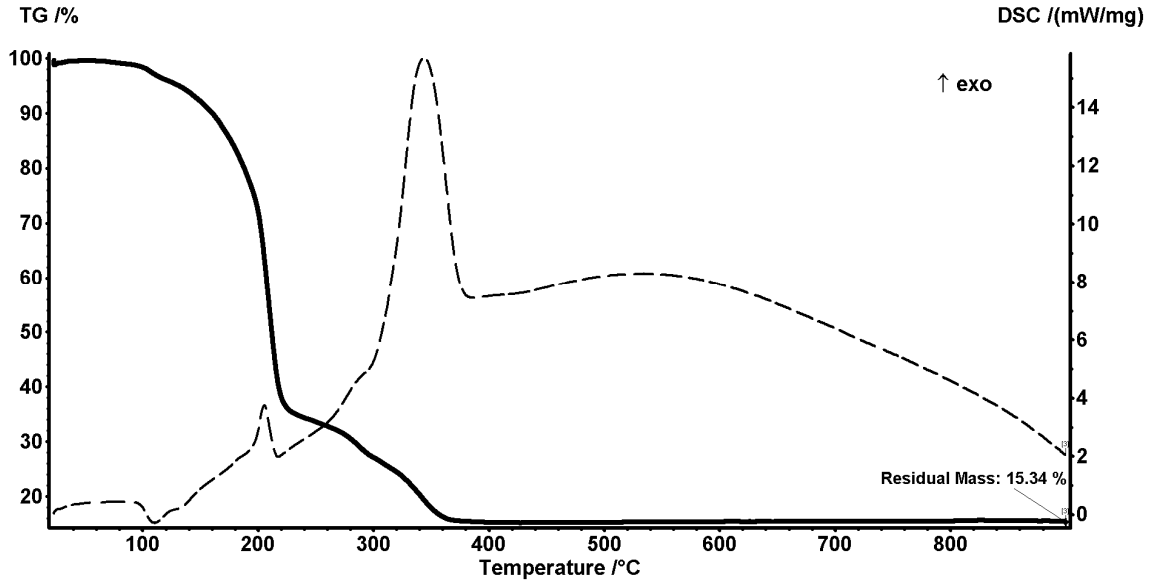

Fig. 2. TG-DTG curves for the obtained xerogel with 5% Gd(III)

The Fig. 3 shows the FT-IR spectra for the Gd(III) doped ZnO (5%) powder obtained by calcination at 400°C. The absorption bands near 3400 cm^{-1} were attributed to O-H stretching

vibration, coming from the surface OH groups and the 1634 cm^{-1} corresponds to water molecules adsorbed on the ZnO nanoparticle's surface. Even if the synthesis is carried out at 400°C not all the surface adsorbed OH groups are removed. In addition, the handling of the nanopowder was done in the ambient atmosphere so there is a possibility that some water molecules to come from the air also. Another two strong absorption bands were observed at 439 and 504 cm^{-1}. The band at 504 cm^{-1} may be associated with oxygen deficiency and/or oxygen vacancy defect complex in ZnO [20]. Changes of oxygen composition can be evaluated also indirectly by variation of intensity of the spectroscopic band at 439 cm^{-1} because this mode involves vibrations of only the oxygen sublattice [21,22]. As air or oxygen annealing of ZnO usually diminishes the Vo defect density, but also increase the number of O_i type defects, we correlate the intensity of these bands with the number of O_i type defects. This increase of O_i type defects should translate into an enhanced green emission in PL spectra.

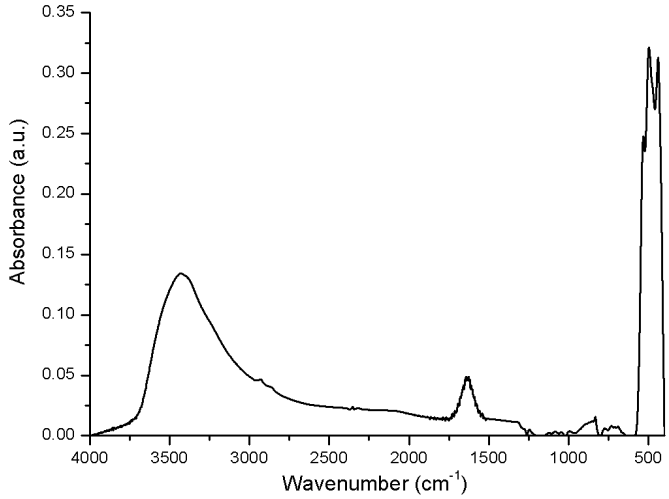

Fig. 3. The FT-IR spectra of Gd (III) doped ZnO nanopowder (5%).

The crystalline phase formation was investigated by X-ray diffraction. The XRD data presented in Fig. 4A sustain also the FTIR data, demonstrating the formation of ZnO as final product [ASTM 80-0075]. All patterns can be indexed to a hexagonal wurtzite structure. The XRD patterns show that there was no second-phase peak and that the doping did not change the wurtzite structure of ZnO. Signals that could be assigned to crystalline Gd, Gd oxide or Zn–Gd alloys particles in the XRD have not been found. However, we cannot rule out the possibility of the formation of precipitates or clusters of secondary amorphous phase small enough not to be detected by the XRD measurements.

The crystallite size of the samples can be estimated from the Scherrer equation, $D = 0.89 \cdot \lambda / \beta \cdot \cos\Theta$, where D is the average grain size, λ is the X-ray wavelength (0.15405 nm), Θ and β are the diffraction angle and FWHM of an observed peak, respectively. The strongest peak (101) was used to calculate the average crystallite size (D) of ZnO particles. The estimated average crystallite size is 34-35nm for all samples.

The lattice constant calculated for ZnO as obtained are a = b = 3.24Å, c = 5.21Å. For the other samples the values are presented in table 1. For the doped samples, the *c* parameter is less in comparison with its value for the undoped ZnO, which suggests that ions Gd^{3+} ions replace the Zn^{2+} lattice sites or interstitial sites in the sample [23]. Although the change is small, the concentration of the dopant plays a role in the variation in the *c*-parameter, which is an indicator for the Gd doping in ZnO.

The Bragg angle of the intense (101) reflection showed a slight shift $\Delta(2\Theta_{101})$ toward higher values relative to that of undoped ZnO. This is evidence for the creation of internal compressive micro stress [24]. This slight peak shift $\Delta(2\Theta_{101})$ is a result of structural strain ($\varepsilon_s = -\Delta\Theta_{(101)} \cot\Theta_{(101)}$), which is of the order of 10^{-2}. This strain is caused by a compressive

microstress (σ_{st}) that can be estimated by: $\sigma_{st} \approx (3\ \varepsilon_s) \cdot B$, where B is the average bulk modulus which is usually about 143 GPa for ZnO [25]. Table 1 show that the obtained values for σ_{st} are in the range of 22.87 to 67.82 GPa, which is less than what is expected for ZnO. Dakhel et al [26] explained this in terms of oxygen vacancies in the ZnO crystalline structure created by the introduction of Gd(III) ions, which decreases its lattice parameters. It is known that the more oxygen is introduced into the crystalline structure, the stronger the resulting tensile stress [27]. Therefore, the sample with 5% Gd should have relatively the largest oxygen-vacancy content, which should be translated in the strongest blue green fluorescence.

Table 1. Lattice parameters and the structural analysis results for the undoped and Gd(III) doped ZnO powders

Sample	Lattice constants (nm)		$2\Theta_{(101)}$	FWHM (101)	D (nm)	ε_s ($\cdot 10^{-2}$)	σ_{st} (GPa)
	a=b	c					
ZnO	0.324	0.521	36.309	0.244	33.8	-	-
ZnO/ Gd 1%	0.324	0.520	36.344	0.241	34.3	5.33	22.87
ZnO/ Gd 2.5%	0.324	0.519	36.379	0.238	34.7	10.65	45.69
ZnO/ Gd 5%	0.323	0.517	36.413	0.237	34.9	15.81	67.82

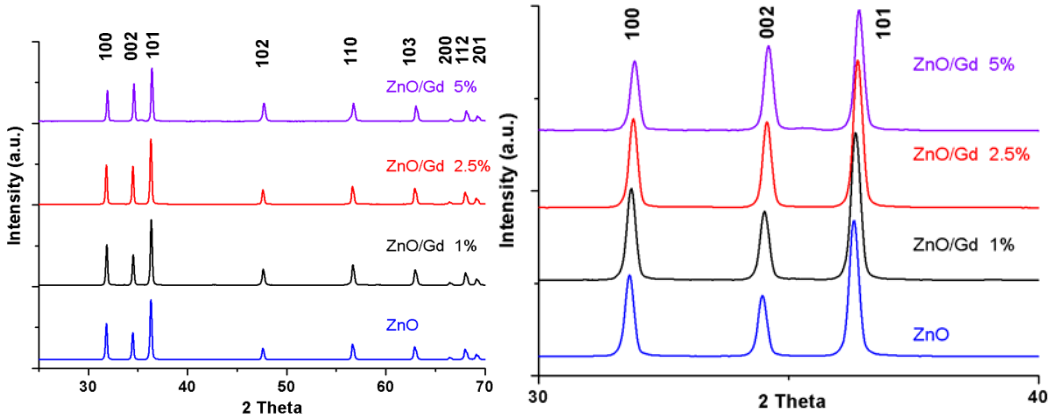

Fig. 4. (A) XRD patterns of undoped ZnO powder and Gd-doped ZnO powder samples at different doping levels 1%, 2.5% and 5%; (B) Detail of the shifting of the Bragg angle of the (101) reflection.

The TEM bright field image, Fig. 5a, of Gd-doped ZnO nanoparticles (5%) obtained after an annealing time of 2 hours at 400^{o}C reveals that the powder is composed from polyhedral shaped particles, with an average particle size of approximately 30 nm. The nanopowder presents a tendency to form agglomerates.

Additional information about the structures of the nanoparticles was found through detailed analysis with HRTEM. The HRTEM image, figure 4b, shows clear lattice fringes of interplanar distances of d = 2.72 Å for nanocrystalline ZnO, corresponding to Miller indices of (1 0 0) crystallographic planes of hexagonal ZnO. In addition, the regular succession of the atomic planes indicates that the nanocrystalites are structurally uniform and crystalline with almost no amorphous phase present.

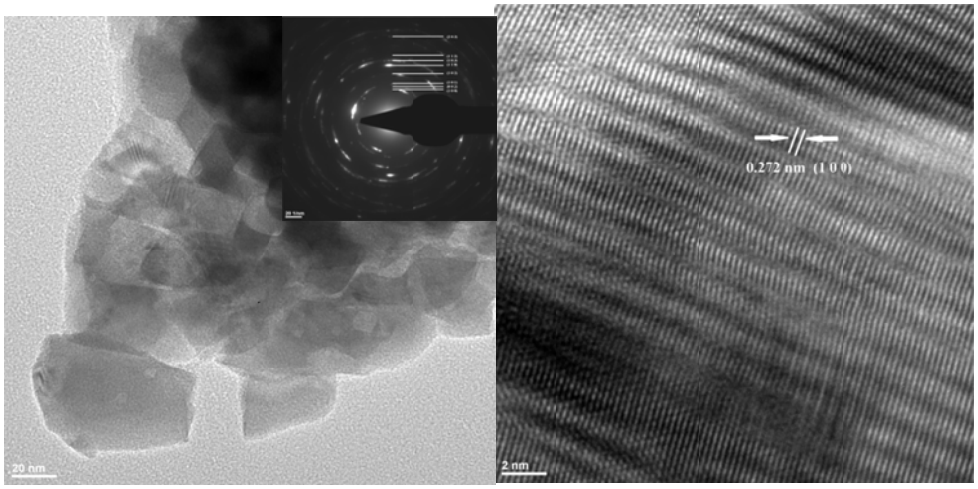

Fig. 5. (a) TEM images of ZnO polyhedral shaped particles obtained by 2 hours annealing at 400°C - SAED pattern of planes of hexagonal structure ZnO [ASTM 80-0075]; (b) HRTEM with the (1 0 0) crystallographic planes of ZnO

From the selected area diffraction pattern obtained on ZnO nanopowder, we can state that the only phase identified is the crystalline hexagonal form of ZnO [ASTM 80-0075]. Moreover, the SAED image of ZnO nanoparticles confirms the Miller indices of characteristic crystalline structures identified by XRD (inset of figure 5a).

The literature is abundant in reports of ZnO photoluminescence. The photoluminescence spectra of ZnO powders usually presents two emission peaks in the UV and visible ranges [28], the relative intensity of which strongly depended on O_2 pressure used during the synthesis process [29].

The UV emission corresponds to the near band-edge emission (NBE) and the visible emission is commonly referred to as a deep-level or trap-state emission [30].

The relative strength of NBE to deep level defect emissions exhibits a dramatic threshold dependence on surface roughness: surface optical emission efficiency increases over tenfold as roughness decreases to unit cell dimensions, highlighting the coupled role of surface morphology and near-surface defects for high efficiency ZnO emitters [31].

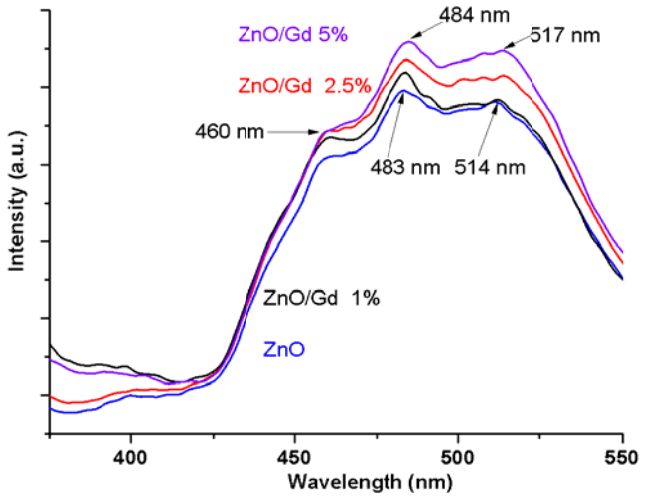

Fig. 6. Photoluminescence spectra of undoped ZnO powder and Gd-doped ZnO powder samples at different doping levels 1%, 2.5% and 5%

High intensity of the green and blue-green luminescence versus NBE are reported in literature whenever the luminescence spectra is recorded on powders as obtained, without further treatments (simple annealing or annealing in presence of reducing atmosphere) [32, 33].

It has been reported that the sub-band-gap emission in ZnO depends on the morphology of the nanostructures. [34-36]. A blue-green emission at 453 nm and a green emission at around 557 nm as found in literature for nest like nanoparticles [35] and emissions at 421 nm, 482 nm, and 532 nm for nanocones [36]. For as nanorods, most of the spectral weight is in the sub-bandgap, centred on 625 nm [32].

The results, figure 6, show that the as-synthesized samples have a wurtzite structure, with a weaker UV emission, and two blue-green emissions, one centred at 484 nm (with a shoulder at 460 nm) and a second at 517 nm. The weak UV emission at 400 nm is assigned to the free exciton emission from the wide band gap of ZnO (NBE). This peak is shifted to 392 nm upon increasing the dopant percentage. The shift in the band edge position is suggested to be due to the influence of Gd doping in ZnO.

The increase in the Gd(III) ions percentage has a direct effect on the intensity of the blue-green emission. The 5% Gd doped ZnO nanopowder present an increase in PL emission with 15%. The increase in intensity takes place systematically, which confirms the occurrence of doping dependence on the intensity. According to literatures, the enhancement of green emission is caused by the removal of electron capture centres on the surface of nanocrystals or the removal of nonradiative decay channels [37, 38]. This behaviour can be correlated with the formation of O_{Zn}, V_{Zn}, O_i defects by dissociation from oxygen-rich states that is responsible for the stronger blue-green band [39,40].

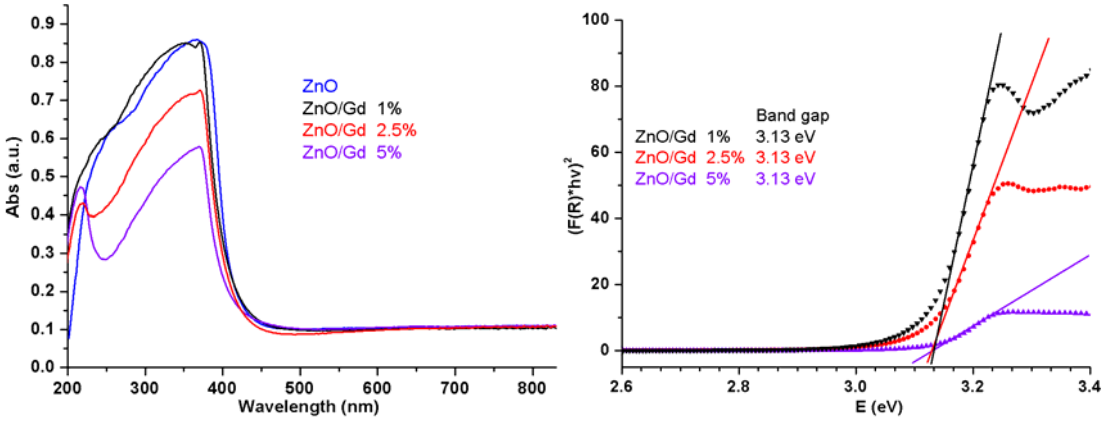

Fig. 7. Diffuse reflectance spectra (A) and plot of the transformed Kubelka-Munk function vs. the energy (B) for the Gd-doped ZnO powder samples at different doping levels 1%, 2.5% and 5%.

The electronic spectra recorded for Gd-doped ZnO powder samples are presented in Fig. 7a.

The fundamental absorption refers to the optical transition of electrons from the valence band to conduction band and can be used to determine the nature and values of optical band gap of the nanoparticles [41, 42]. For analysis purposes the diffuse reflectance, *R*, of the sample can be related to the Kubelka-Munk function *F(R)* by the relation $F(R)=(1-R)^2/2R$, [43]. To determine the band-gap energies (Eg) for the Gd-doped ZnO powder samples, a plot of the square of the modified Kubelka-Munk function vs. the energy is presented in the figure 7b. This yields the direct band gap energy. Adopting the method proposed by Cao et al.,[44] the band-gap energies (Eg) for the Gd-doped ZnO powder samples are determined to be 3.13 eV, by the extrapolation to $[F(R)\cdot h\nu]^2 = 0$. The calculated band gap for the Gd-doped ZnO powder samples is smaller than that for pure ZnO, which is in good agreement with the fact that doping ions will introduce new electronic levels inside the ZnO band gap.

Magnetization curves as a function of applied magnetic field (M-H) at RT of samples are revealed in Fig. 8, where the contributions of the paramagnetism (PM) signals of the samples were deducted.

Due to the partially filled f-orbitals that carry magnetic moments, RE ions may take part in magnetic coupling like TM with partially filled d-orbitals. While is expected that the magnetic

coupling strength of d-orbitals to be greater than those of f-orbitals, Gd(III) presents both 5d and 4f partially filled orbitals. So both can take part via intra-ion 4f-5d exchange interaction followed by inter-ion 5d-5d coupling mediated by charge carriers.

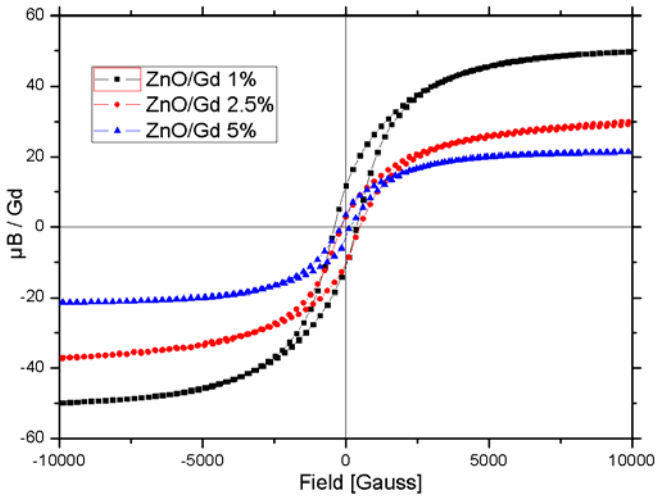

Fig. 8. The magnetization vs magnetic field curves for the Gd-doped ZnO powders.

It can be seen that the doped samples exhibit hysteresis curves with the different saturation magnetization (Ms), which indicates that all the doped samples have the clear RTFM. It's sure that the RTFM is induced by doping of Gd(III). Furthermore, the magnetism of the samples depends strongly on the doping Gd(III) content, and Ms per Gd(III) ion decreases monotonously from 49 μB/Gd ($Zn_{0.99}Gd_{0.01}O$) to 21 μB/Gd ($Zn_{0.95}Gd_{0.05}O$) as the increase of the doping content. This could be due to antiferromagnetic alignment caused by the increased number of Gd atoms occupying adjacent cation positions. A similar effect was observed in Co-doped ZnO [45] and Er-doped ZnO [46] systems. Our magnetization measurements reveal a high magnetic moment of up to 49 μB per Gd atom. This huge magnetic moment can be understood in terms of a long-range spin polarization of the ZnO matrix by Gd.

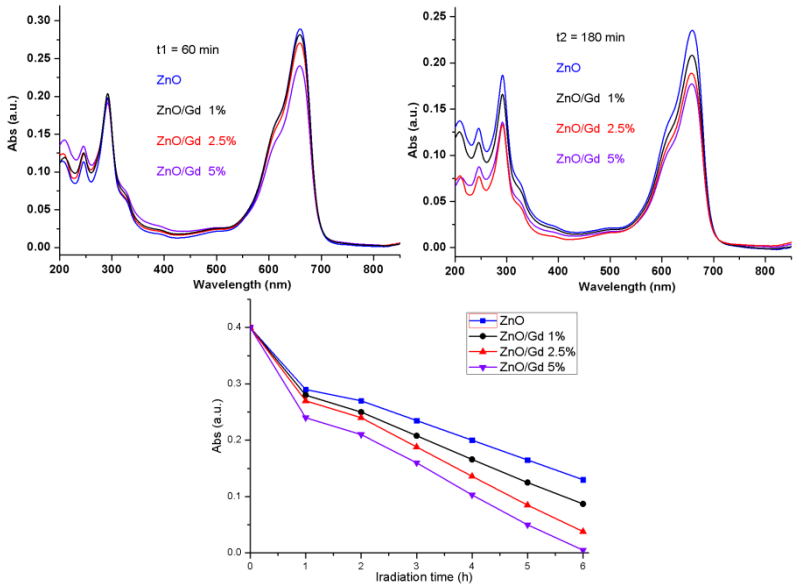

Fig. 9. Determination of photocatalytic activity of undoped ZnO powder and Gd-doped ZnO powder samples versus methylene blue: a) after 60 min; b) after 180 min; c) comparative evolution of absorption maximum (658nm) vs irradiation time.

Like many thiazine dyes, MB has a tendency to dimerise. The dimer of MB, (MB)2, has an absorption maximum at 614 nm [47] vs 658 nm for the monomer MB [48]. The decreases of both absorption maximums indicate that all samples have a photocatalytic activity. As the results indicate, figure 9, all the Gd-doped samples have a better activity than undoped ZnO powder. The increase in the Gd(III) percentage in the ZnO nanopowders leads to an increasing photocatalytic activity. As XRD results indicate only a minor increase in grain size, we can attribute this increase activity directly to the formation of more surface defects as Gd(III) percent increase. These results are confirming the conclusions from photoluminescence analysis.

5. Conclusions

A synthetic method for the undoped ZnO and Gd-doped ZnO nanocrystalline powder using starch has been presented. The sol-gel process produces a xerogel that was calcinated at 400^{o}C for 2 hours. The Gd(III) ions were incorporated in the ZnO lattice, XRD analysis indicating existence of a single phase compound, wurtzite. The samples exhibited blue-green photoluminescence by the UV excitation, the presence of Gd(III) enhancing the emission. TEM and XRD data sustain the formation of a single phase, monodisperse crystalline Gd-doped ZnO nanopowder. The band gap value of doped samples is smaller than the band gap value of the bulk ZnO. All samples exhibit an unusually high value of μB per Gd atom, but the value decrease as we increase the percent of the doping ion.

The samples exhibited blue-green photoluminescence by the UV excitation, the presence of Gd(III) enhancing the emission. Also with increasing of Gd(III) percent, we notice an increase in the photocatalytic activity. Both effects, enhanced luminescence and better photocatalytic activity can be explained by an increasing in the surface defects associated with lattice distortion induced by Gd(III) ions.

Acknowledgments

Authors recognize financial support from the European Social Fund through POSDRU/89/1.5/S/54785 project: "Postdoctoral Program for Advanced Research in the field of nanomaterials"

References

[1] Weißenrieder, K.S. and Muller, J. Thin Solid Films, **300**, 30-41 (1997).
[2] Masai, H., Toda, T., Ueno, T., Takahashi, Y. and Fujiwara, T. Appl. Phys. Lett., **94**, 151908 (2009).
[3] Behnajady, M. A., Modirshahla, N., Ghazalian E. Digest Journal of Nanomaterials and Biostructures, **6**(1), 467-474 (2011).
[4] Lorenz, C., Emmerling, A., Fricke, J., Schmidt, T., Hilgendorff, M., Spanhel, L., Muller, G., J. Non-Cryst. Solids, 238, 1 (1998)
[5] Radu, A., Iftimie, S., Ghenescu, V., Besleaga, C., Antohe, V.A., Bratina, G., Ion, L., Craciun, S., Girtan, M., Antohe, S. Digest Journal of Nanomaterials and Biostructures, **6**(3), 1141-1148 (2011).
[6] Gupta, A., Bhatti, H.S., Kumar, D., Verma, N.K., Tandon, R.P. Digest Journal of Nanomaterials and Biostructures, **1**(1), 1 -9 (2006).
[7] A. A. Dakhel, M. El-Hilo, JOURNAL OF APPLIED PHYSICS **107**, 123905 (2010).
[8] M. Subramanian, P. Thakur, M. Tanemura, T. Hihara, V. Ganesan, T. Soga, K. H. Chae, R. Jayavel, T. Jimbo, JOURNAL OF APPLIED PHYSICS **108**, 053904 (2010).
[9] K. Potzger, S. Zhou, F. Eichhorn, M. Helm, W. Skorupa, A. Mucklich, J. Fassbender, J. Appl. Phys. **99**, 063906 (2006).
[10] J. Qi, Y. Yang, Li Zhang, J. Chi, D. Gao, and D. Xue, Scr. Mater. **60**, 289 (2009).
[11] S. Zhou, K. Potzger, A. Mucklich, F. Eichhorn, M. Helm, W. Skorupa, J. Fassbender, Nucl. Instrum. Methods Phys. Res. B **266**, 589 (2008).
[12] F. Pan, C. Song, X. J. Liu, Y. C. Yang, and F. Zeng, Mater. Sci. Eng. R. **62**, 1 (2008).

[13] S. K. Mandal, A. K. Das, T. K. Nath, and D. Karmakar, Appl. Phys. Lett. **89**, 144105 (2006).
[14] B. B. Straumal, A. A. Mazilkin, S. G. Protasova, A. A. Myatiev, P. B.Straumal, B. Baretzky, Acta Mater. **56**, 6246 (2008).
[15] A.F. Kohan, G. Ceder, D. Morgan, Chris G. Van de Walle, Phys. Rev. B. **61** 15019 (2000).
[16] Hsieh, P.T., Chen, Y.C., Kao, K.S., Wang, C.M., Appl. Phys. A **90**, 317–321 (2008)
[17] Wagner, C.D. Farad. Discuss. Chem. Soc., **60**, 291 (1975)
[18] Futsuhara, M., Yoshioka, K., Takai, O. Thin Solid Films **322**, 274 (1998).
[19] O. Oprea, E. Andronescu, B.S. Vasile, G. Voicu, C. Covaliu, Dig J Nanomater Bios. **6**, 1393-1401 (2011).
[20] A. Kaschner, U. Haboeck, M. Strassburg, M. Strassburg, G. Kaczmarczyk, A. Hoffmann, C. Thomsen, A. Zeuner, H.R. Alves, D.M. Hofmann, B.K. Meyer, Appl. Phys. Lett. **80**, 1909 (2002).
[21] G. Xiong, U. Pal, J.G. Serrano, K.B. Ucer, R.T. Williams, Phys. Stat. Sol. (C) **3**, 3577–3581 (2006).
[22] A. Djelloul, M-S. Aida, J. Bougdira, Journal of Luminescence **130**, 2113–2117 (2010).
[23] Q. Yu, W. Fu, C. Yu, H. Yang, R. Wei, Y. Sui, S. Liu, Z. Liu, M. Li, G. Wang, C. Shao, Y. Liu, G. Zou, J. Phys. D **40**, 5592 (2007).
[24] A. A. Dakhel, M. El-Hilo, JOURNAL OF APPLIED PHYSICS **107**, 123905 (2010).
[25] C. F. Cline and D. R. Stephens, J. Appl. Phys. **36**, 2869 (1965).
[26] A. A. Dakhel, M. El-Hilo, JOURNAL OF APPLIED PHYSICS **107**, 123905 (2010).
[27] W. Zhaoyang, H. Lizhong, Vacuum **83**, 906 (2009).
[28] Tian, Z.R., Voigt, J.A., Liu, J., Mckenzie, B., Mcdermott, M.J., Rodriguez, M.A., Konishi, H., Xu, H.F. Nat. Mater. 2, 821 (2003).
[29] Bae, C.H., Park, S.M., Park, S.C. and Ha, J.S. Nanotechnology **17**, 381–384 (2006).
[30] Huang, M.H., Wu, Y., Feick, H., Tran, N., Weber, E. and Yang, P. Adv. Mater. **13**, 113 (2001)
[31] Doutt, D., Mosbacker, H. L., Cantwell, G., Zhang, J., Song, J.J. and Brillson, L. J. Applied Physics Letters **94**, 042111 (2009).
[32] Hsu, J.W.P., Tallant, D.R., Simpson, R.L., Missert, N.A. and Copeland, R.G. Applied Physics Letters **88**, 252103 (2006).
[33] Yuldashev, Sh. U., Sung Woo Choi and Tae Won Kang Journal of the Korean Physical Society, **42**, S216_S218 (2003).
[34] Kwok, W. M., Djurisic, A. B., Leung, Y. H., Chan, W. K. and Phillips, D. L. Appl. Phys. Lett. **87**, 223111 (2005).
[35] Li Yan, Feng Hui-yun, Zhang Nan, Liu Chuan-sheng, Trans. Nonferrous Met. Soc. China **20**, 119−122 (2010).
[36] Zhang, D. H., Wang, Q. P. and Xue, Z. Y. Appl. Surf. Sci. **207**, 20 (2003)
[37] Zhang, Y., Li, Y.D. J. Phys. Chem. B **108**, 17805 (2004).
[38] Liu Wentan Ren, Yong Zhang, Yin-Xi Zhang European Polymer Journal **47**, 1135–1141 (2011).
[39] X. M. Fan, J. S. Lian, Qing Jiang, ZuoWan Zhou, J Mater Sci. **42,** 2678–2683 (2007).
[40] Ming-Kwei Lee, Hwai-Fu Tu, Jpn. J. Appl. Phys. **47**, 980-982 (2008).
[41] Rozati, S.M., Shadmani, E. Digest Journal of Nanomaterials and Biostructures **6**(2), 365-372 (2011).
[42] Singh, S., Kaur, H., Pathak, D., Bedi, R.K. Digest Journal of Nanomaterials and Biostructures **6**(2), 689 – 698 (2011).
[43] Kortum, G. Reflectance Spectroscopy; Springer-Verlag: New York (1969).
[44] Cao, G., Rabenberg, L. K., Nunn, C. M., Mallouk, T.E. Chem. Mater. **3**, 149–156 (1991).
[45] M. Venkatesan, C. B. Fitzgerald, J. G. Lunney, and J. M. D. Coey, Phys. Rev. Lett. **93**, 177206 (2004).
[46] J. Qi, Y. Yang, L. Zhang, J. Chi, D. Gao, and D. Xue, Scr. Mater. **60**, 289 (2009).
[47] Mills, A. and J. Wang, J. Photochem. And Photobiol. A: Chemistry **127**, 123-134 (1999).
[48] ISO/DIS 10678: Fine ceramics (advanced ceramics, advanced technical ceramics): Determination of photocatalytic activity of surfaces in an aqueous medium by degradation of methylene blue, standard under development